Title

Drought impacts on terrestrial primary production underestimated by satellite monitoring

Journal

Nature Geoscience, 12(4)

ISSN

1752-0894

Authors

Stocker, Benjamin D
Zscheischler, Jakob
Keenan, Trevor F
et al.

Publication Date

2019-04-01

DOI

10.1038/s41561-019-0318-6

Peer reviewed

Drought impacts on terrestrial primary production underestimated by satellite monitoring

Benjamin D. Stocker[1]*, Jakob Zscheischler[2,7], Trevor F. Keenan[3,4], I. Colin Prentice[5], Sonia I. Seneviratne[2] and Josep Peñuelas[1,6]

[1] Global Ecology Unit, CREAF, Bellaterra (Cerdanyola del Vallès), Catalonia, Spain. [2] Institute for Atmospheric and Climate Science, ETH Zurich, Zurich, Switzerland. [3] Earth and Environmental Sciences Area, Lawrence Berkeley National, Lab, Berkeley, CA, USA. [4]Department of Environmental Science, Policy and Management, UC Berkeley, Berkeley, CA, USA. [5] Biosphere and Climate Impacts, Department of Life Sciences, Imperial College London, Ascot, UK. [6]CSIC, Global Ecology Unit CREAF-CSIC-UAB, Bellaterra, Spain. [7] Present address: Climate and Environmental Physics, University of Bern, Bern, Switzerland. *e-mail: b.stocker@creaf.uab.cat

Abstract

Satellite retrievals of information about the Earth's surface are widely used to monitor global terrestrial photosynthesis and primary production and to examine the ecological impacts of droughts. Methods for estimating photosynthesis from space commonly combine information on vegetation greenness, incoming radiation, temperature and atmospheric demand for water (vapour-pressure deficit), but do not account for the direct effects of low soil moisture. They instead rely on vapour-pressure deficit as a proxy for dryness, despite widespread evidence that soil moisture deficits have a direct impact on vegetation, independent of vapour-pressure deficit. Here, we use a globally distributed measurement network to assess the effect of soil moisture on photosynthesis, and identify a common bias in an ensemble of satellite-based estimates of photosynthesis that is governed by the magnitude of soil moisture effects on photosynthetic light-use efficiency. We develop methods to account for the influence of soil moisture and estimate that soil moisture effects reduce global annual photosynthesis by ~15%, increase interannual variability by more than 100% across 25% of the global vegetated land surface, and amplify the impacts of extreme events on primary production. These results demonstrate the importance of soil moisture effects for monitoring carbon-cycle variability and drought impacts on vegetation productivity from space.

Main

Accurate estimates of photosynthesis and vegetation primary production across large spatial scales are required for monitoring yields in agriculture and forestry and for understanding drivers of the terrestrial carbon (C) balance and changes in the C cycle. In particular, the severity of drought impacts in natural and managed ecosystems is of wide societal relevance. These impacts are largely determined by the sensitivity of ecosystem-scale apparent photosynthesis (gross primary production, GPP) and plant mortality in response to dry conditions[1]. Remote sensing data-driven models (RS

models) are widely used for estimating GPP[2,3] and underlie research on the impacts of drought on global[4] and continental primary production[5], vegetation recovery from drought[6] and the drivers of recent trends in the terrestrial C balance[7,8], for example. RS models commonly rely on the light-use efficiency (LUE) concept[9], which states that, at timescales of weeks to months, GPP can be formulated as the product of the incident photosynthetically active radiation (PAR), the fraction of absorbed PAR (fAPAR) and the LUE[9]:

$$\mathrm{GPP} = \mathrm{PAR} \times \mathrm{fAPAR} \times \mathrm{LUE} \quad (1)$$

This formulation robustly captures the relationship between GPP and light through PAR. It also incorporates effects of changes in green vegetation cover through fAPAR, which reflects water and temperature-driven phenology and captures the lagged responses of plant mortality and ecosystem structural change induced by drought. Biome-level differences and responses of leaf-level physiology to ambient conditions are represented by the LUE, which is commonly modelled using information on vegetation type and takes effects of changes in air or land-surface temperature and vapour-pressure deficit (VPD) into account.

Although low soil moisture is known to affect plant physiology[10,11,12], RS models commonly assume that the information contained in fAPAR and VPD is sufficient to accurately estimate the responses of GPP to drought[13]. However, deficits in soil moisture and their effects on GPP are not necessarily captured by fAPAR or VPD. VPD progressively decouples from soil moisture under very dry conditions[14,15], and GPP can become decoupled from fAPAR during soil moisture droughts due to stomatal and biochemical responses and the resulting variations in LUE[16]. Recent research has emphasized that both drivers of dryness effects, VPD and soil moisture, should be accounted for to explain and simulate observed changes in ecosystem fluxes and LUE[17,18,19,20,21].

Here, we use a set of state-of-the-art RS models that follow different approaches for simulating GPP and dryness effects. Common to all of them is that soil moisture is not explicitly used as a model input nor accounted for as a model variable. Model predictions are evaluated using data from a globally distributed network of ecosystem flux measurements. We show that all of the RS models assessed exhibit a similar bias under dry conditions and that this bias matches the timing and magnitude of the apparent soil moisture-related reduction in LUE (termed fLUE). To quantify the soil moisture effect, separate from other drivers, we use an estimate of fLUE by ref. [20] that combines observations and a machine-learning algorithm. We demonstrate that the bias in the GPP estimates of the RS models can largely be resolved by empirical methods that are based on readily available global datasets and simple soil water-balance models. We use these methods in combination with an RS model (P-model[22]) to assess the implications of including soil-

moisture stress for GPP across the globe, its interannual variability and the probability of large negative GPP extreme events.

Resolving the bias

We find a consistent pattern in the bias of GPP estimated from RS models that is due to the timing and magnitude of drought impacts on GPP (Fig. 1a). In all of the RS models assessed using data from 36 sites (see Supplementary Table 1 and Supplementary Fig. 1), the bias progressively increases during the course of droughts and closely tracks the apparent impacts of soil moisture on LUE, estimated by fLUE[20]. This is also reflected by the systematic relationship between the bias and the magnitude of fLUE (Fig. 1b). We also investigated the relationships between the model bias and drought impacts for an extended set of sites ($N = 71$), relaxing the requirement that fLUE data is available, which is satisfied only for 36 sites. Instead of using fLUE data, we estimate the severity of drought impacts by the daily ratio of actual evapotranspiration to potential evapotranspiration (AET/PET) derived from the water and energy balance of the land surface[23]. The same pattern emerges (Supplementary Fig. 2) and confirms that these RS models systematically underestimate the impacts of drought on GPP.

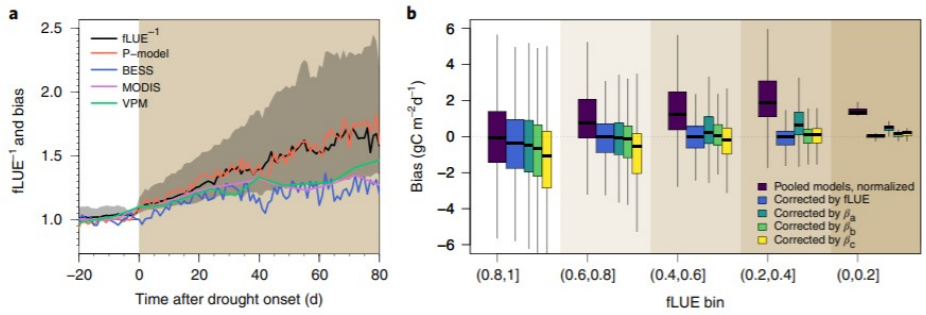

Fig. 1 | Bias in GPP estimates. a, Bias in GPP simulated by different RS models, and apparent effects of soil moisture on LUE (inverse of fLUE) during drought events. The bias is expressed here as the ratio of simulated over observed GPP. Lines represent the median for each day, derived from 36 sites (group 1 in Supplementary Table 1) and multiple drought events. The grey band is the interquartile range of fLUE^{-1}. Bias values are normalized to a median of 1 for the 20 d before the onset of drought events. **b**, Bias in simulated daily GPP for different fLUE bins, calculated as the simulated minus observed GPP at 36 sites (group 1 in Supplementary Table 1). Uncorrected data from the different RS models are pooled and normalized to the median ratio of simulated/observed GPP in the highest fLUE bin (0.8–1.0). Pooled and normalized data are multiplied by fLUE[20] and empirical soil moisture stress functions with different sensitivities. The brown shading (**b**) illustrates increasing soil moisture stress. Boxes represent the interquartile ranges of the values (Q_{25}, Q_{75}), and whiskers cover Q_{25}-1.5×(Q_{75}-Q_{25}) to Q_{75}+1.5×(Q_{75}-Q_{25}).

This bias is common to all of the RS models assessed here (MODIS MOD17A2H[3], VPM[24], BESS[25], P-model[22]). MODIS, VPM, and BESS tend to underestimate GPP under moderate soil-moisture stress and have a tendency towards a positive bias with increasing soil-moisture stress (Supplementary Fig. 3), which balances errors and reduces the overall bias in estimates for mean GPP across all levels of soil dryness. We normalized simulated GPP to levels where impacts of soil moisture are small, distilling the common general pattern of an increasingly positive bias in simulated GPP as soil moisture progressively reduces LUE, shown in Fig. 1. The bias for each individual RS model is shown in Supplementary Fig. 4.

These findings imply that accurately estimating the degree to which soil moisture reduces LUE and GPP, in addition to the effects of greenness (fAPAR), VPD and other factors, could resolve the systematic bias and reduce errors in GPP estimates across all levels of dryness. The power of this bias correction is illustrated by the near complete disappearance of the bias and a substantial reduction in the error of normalized GPP values, simulated by RS models, after correction by fLUE (blue boxes in Fig. 1b; the mean bias decreases from 1.65 to 0.031 $gC\,m^{-2}\,d^{-1}$ and the root mean squared error decreases from 2.52 to 0.94 $gC\,m^{-2}\,d^{-1}$ across the lower four fLUE bins).

Global implications

To assess the implications of the drought-related bias in RS estimates of GPP across the globe and its variability, we constructed a set of empirical soil moisture stress functions (termed β functions) based on the apparent soil moisture impacts on LUE derived from local measurements[20]. In combination with accessible data, which has coverage spanning the globe and the entire satellite era (here 1982–2016), these β functions thus provide a basis for upscaling in time and space. Plant-available soil moisture, used as input to the β functions, is estimated from the surface water and energy balance[23], using daily precipitation and radiation data and a high-resolution soil dataset[26]. Three β functions (termed β_a, β_b and β_c) are parameterized with different levels of sensitivity to low soil moisture and using information on vegetation type and mean aridity (see Methods). The range of the β functions generally covers the estimated range of soil moisture effects on LUE (Supplementary Fig. 5). Correcting simulated GPP from the RS models using the intermediate β function (β_b) reduces the mean bias from 1.65 to 0.25 $gC\,m^{-2}\,d^{-1}$ and the root mean squared error from 2.52 to 1.32 $gC\,m^{-2}\,d^{-1}$ during droughts—that is, across the lower four fLUE bins (green boxes in Fig. 1b).

Next, we conducted global simulations to investigate effects of soil moisture stress on GPP, its temporal trend, interannual variability and negative GPP extreme events. We use the P-model (see Methods), where fAPAR is prescribed by satellite observations[27] and LUE is simulated on the basis of an optimality principle that accounts for climate and CO_2 effects on the balance between costs of assimilation and transpiration[22]. By quantifying the difference in variables from a simulation without β functions (termed s0) and three alternative simulations that include β functions (s1a, s1b and s1c using functions β_a, β_b and β_c, respectively), we isolate soil moisture effects from other environmental and anthropogenic drivers.

We find that soil moisture stress reduces global GPP on average by 15% (10–19%, based on different simulations; see Fig. 2 and Supplementary Fig. 6). Local effects in semi-arid grasslands and savannahs are larger, reducing mean annual GPP by more than 50%. The correction made by applying the β functions in P-model simulations improves its performance for simulating spatial (that is, across-site) variations in mean annual GPP

(Supplementary Figs. 7 and 8), and brings global totals closer to estimates by other RS models (Fig. 2b). We find no significant temporal trend in the soil moisture-related relative reduction in global GPP over the last 30 years, but significant positive and negative trends in different regions (Fig. 2c,d). While the Sahel region, southern Africa and northern Australia have seen a trend towards relief from soil moisture stress, simulated GPP reductions have become increasingly strong in the Gran Chaco in South America, the Middle East and in the dry regions of Mexico and Southwestern United States.

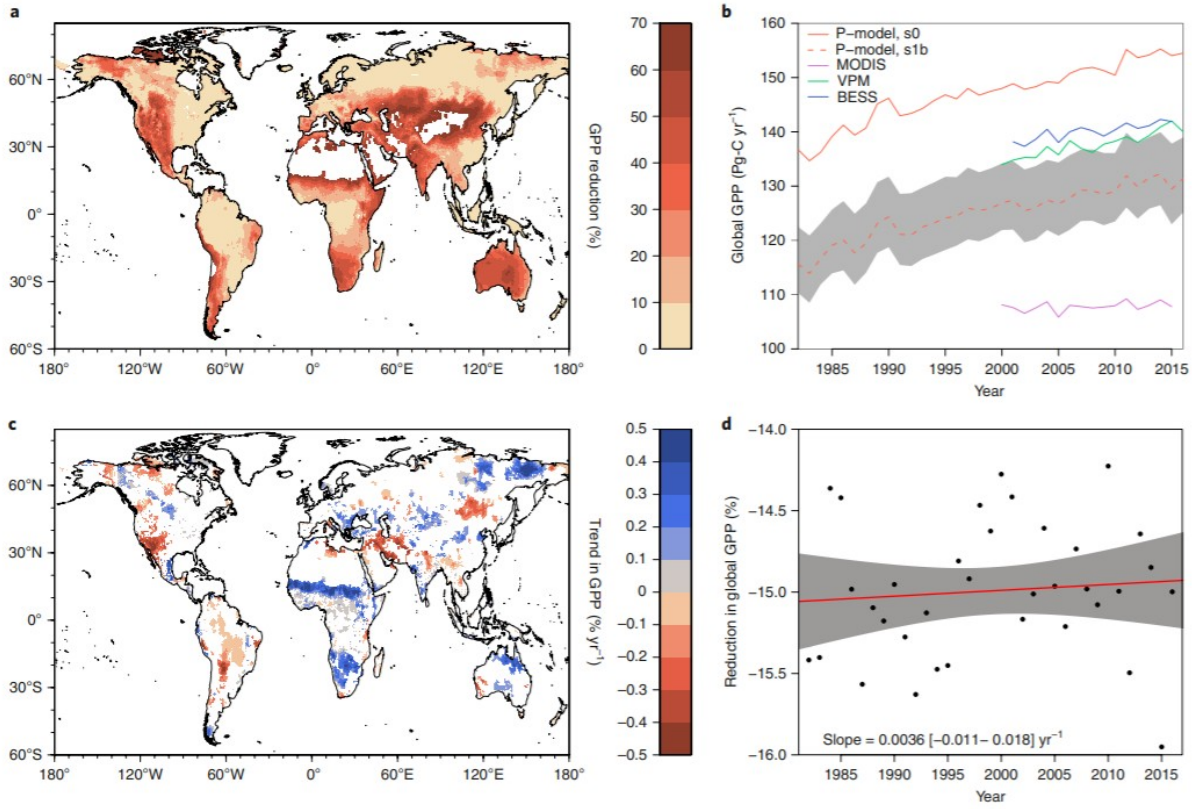

Fig. 2 | Effect of soil moisture limitation on GPP. a, GPP reduction due to the effects of soil moisture, calculated as the difference in the mean for 1982–2016 from simulations s0 and s1b. **b**, Time series of global GPP from different RS models. The grey envelope represents the range of simulations s1a and s1c. **c**, Trend in soil moisture impacts on GPP, calculated as the linear trend in the percentage difference in annual GPP from simulations s0 and s1b, covering 1982–2016. Blank gridcells indicate no significant trend, red shades indicate a trend towards stronger GPP reductions by soil moisture effects. **d**, Percentage difference in global annual GPP from simulations s0 and s1b. The linear regression is plotted as the red line, with the shaded envelope indicating the 95% confidence interval; the slope with its 95% confidence interval are also given.

Soil moisture effects on GPP variability across scales

Soil moisture limitation not only affects mean annual GPP, but also its interannual variability (IAV). The IAV in precipitation and hence soil moisture increases GPP IAV across all vegetated land (Fig. 3). Relative variability (quantified as the variance in annual GPP divided by its mean) increases by more than 100% (doubling) across 25% of the global vegetated land surface. The mean amplification factor across all grid cells is 1.8 (80% increase), with the largest effects of soil moisture on relative and absolute (Supplementary Fig. 9) GPP variability occurring in regions of intermediate aridity (Supplementary Fig. 10).

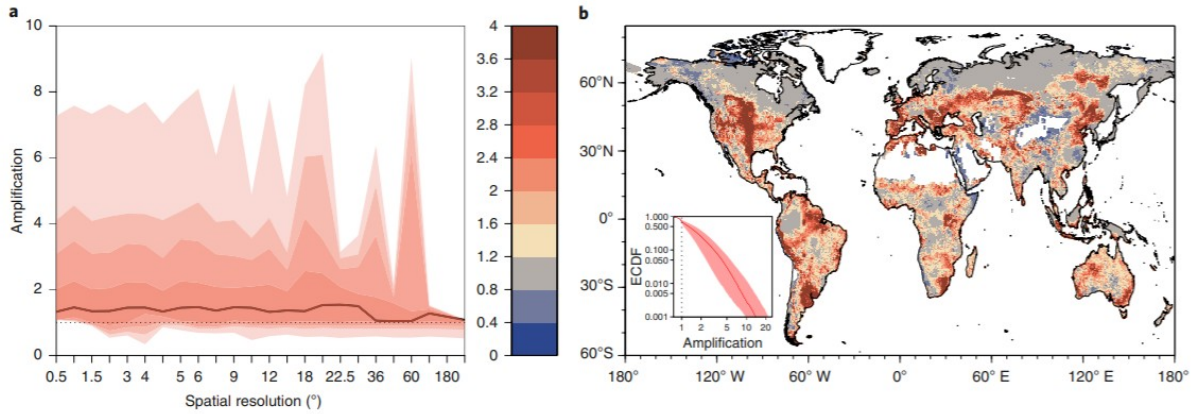

Fig. 3 | Amplification of GPP IAV due to the effects of soil moisture. IAV is calculated as the variance in annual values divided by their mean; amplification is calculated as the ratio of the IAV in simulation s1b to that in s0. **a**, Distribution of amplification factors (unitless) depending on the spatial resolution of aggregation. Shaded bands are the upper and lower 1, 5, 10 and 25% quantiles, and the solid line is the median. The horizontal dotted line at 1 indicates no amplification. **b**, Amplification of GPP IAV across the globe (colour scale, upper limit includes values greater than four). The inset shows the empirical cumulative distribution function (ECDF) of the amplification factors for all grid cells. The solid line represents amplification factors derived from simulation s1b, the shaded red band covers the range of values for simulations s1a and s1c. The dotted vertical line at 1 indicates no amplification.

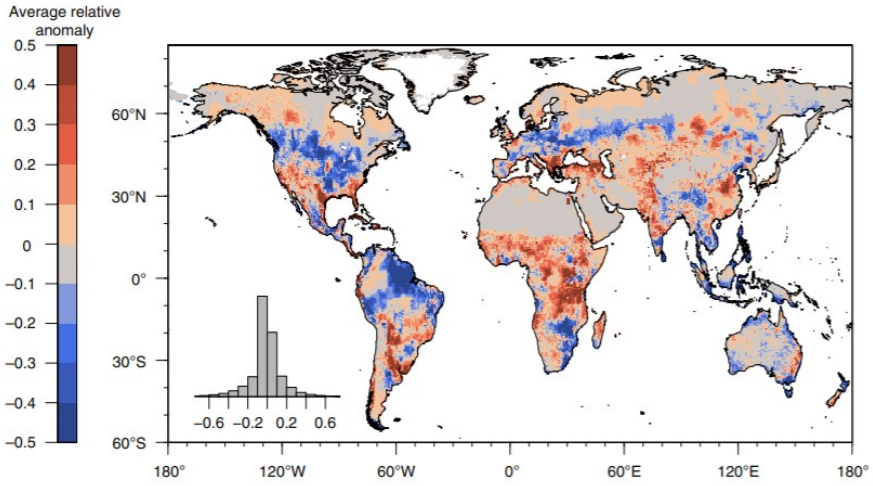

Fig. 4 | Contributing regions where the effects of soil moisture increase and reduce global GPP IAV. Values are based on the detrended annual GPP anomalies of years 1982–2016 and calculated following ref. [55] (see Methods and equation (4)), are unitless and are multiplied by 10,000 for readability. Inset, histogram showing the distribution of the values.

Although the effects of soil moisture substantially increase GPP IAV locally, its effects on the IAV of total global GPP are found here to be minor. The mean amplification decreases from a factor of 1.8, derived from model simulations at a spatial resolution of 0.5° in longitude and latitude, to 1.3 when annual GPP is aggregated to 180° and to 1.08 at the global level (Fig. 3a). This decrease is due to compensating contributions from different regions across the globe (Fig. 4). Positive contributions, where the effect of soil moisture on GPP is in phase with global GPP IAV, are compensated by negative contributions. The frequency distribution of these contributions is approximately symmetrical, hence they balance out at the global scale.

The impacts of climatic extremes on natural and managed ecosystems are strongly governed by GPP anomalies that simultaneously occur across large regions and that persist over extended periods of time[1,28,29]. Most of such large-scale GPP extreme events are associated with precipitation deficits[29]. Here we find that water limitation increases the magnitude of such GPP extreme events (Fig. 5). Although the shape of the size distribution of individual events is largely conserved (minor changes in the power-law exponent related to soil moisture effects), their distributions are generally shifted towards larger sizes. By also accounting for soil moisture effects, the probability of GPP extreme events of a given size increases by 16–66%, with the largest amplification in Australia. Our approach implies that anomalies and impacts are not larger by definition when soil moisture stress is accounted for. However, our results indicate that the effects of soil moisture amplify GPP variability and the magnitude of temporally and spatially clustered negative anomalies.

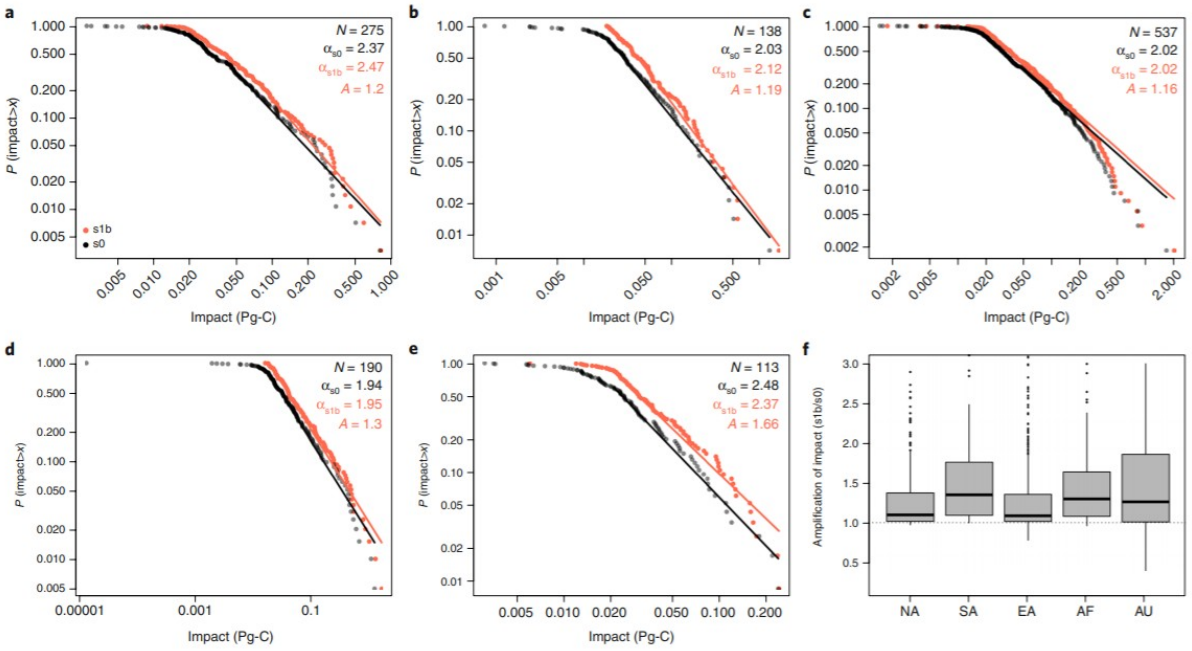

Fig. 5 | Soil moisture effects on GPP extreme events. a–e, Cumulative size distribution of the largest *N* GPP extreme events by continent (note the logarithmic scales of both axes). **a**, North America. **b**, South America. **c**, Eurasia. **d**, Africa. **e**, Australia. Impact represents the cumulative negative GPP anomaly across contiguous regions in space and time for the largest *N* events following the method of ref. [57] (see also Methods). *N*, exponents of fitted power law distributions α and the mean soil moisture-related amplification of the probability for a given event size (*A*) are indicated. *A* is calculated from the events as fitted by the power law distributions (mean upward shift of the distribution of events as estimated by the solid straight lines) derived using the R package poweRlaw[58]. **f**, The distribution of amplification factors for the sizes of individual events on each continent. The bold lines within the boxes are the medians and the boxes are the interquartile ranges (Q_{25}, Q_{75}), and whiskers cover Q_{25}-1.5×(Q_{75}-Q_{25}) to Q_{75}+1.5×(Q_{75}-Q_{25}). NA, North America; SA, South America; EA, Eurasia; AF, Africa; AU, Australia.

Discussion

Multiple studies have indicated that RS models tend to overestimate vegetation productivity under dry conditions[30,31,32,33], but precise quantitative insights into this bias regarding its timing, magnitude, underlying causes and implications for global GPP estimates have been lacking. We used an observation-based estimate of separate soil moisture effects (fLUE[20]) for

comparison with the bias in the GPP estimates of RS models and to formulate and calibrate β functions. The strong bias reduction achieved by including β functions in GPP estimates suggests that soil moisture effects on LUE, in addition to VPD and greenness changes, drive the progressive overestimation in GPP during droughts. The remaining bias may be reduced by accounting for additional factors that are known to affect the sensitivity of vegetation productivity to dry soil conditions, such as groundwater access[34,35], but are not included in the RS models investigated here, nor in β functions[36].

RS models are typically calibrated to minimize errors compared to CO_2 flux-derived GPP estimates. While this yields relatively accurate annual mean GPP estimates across sites[22,37], it tends to underestimate GPP under moist conditions and overestimate it under dry conditions, as shown here. This also indicates that the tendency of RS models to overestimate GPP under droughts does not necessarily imply a general overestimation of annual or global totals. However, the systematic relationship of their bias with soil moisture limits the potential to minimize overall errors. Furthermore, our results demonstrate that the systematic bias implies a substantial underestimation of the IAV of GPP and the impacts of extreme droughts on GPP. However, this does not have direct implications for estimates of the global land C balance, as GPP data are not commonly used for this purpose[38].

To remediate the drought-related bias in GPP estimates, attempts have been made to use remotely sensed surface reflectance data to estimate water availability[39,40] or to directly measure physiological responses to water stress and the resulting changes in LUE. An index of surface water availability is implemented in VPM but does not resolve its bias under water-stressed conditions. Empirical relationships between LUE and atmospheric dryness (VPD), as implemented in MODIS, may partly account for soil moisture effects but are limited by a lack of correlation between VPD and soil moisture that is particularly prevalent under very dry conditions[14,15,20]. BESS and the P-model implement standard process-based models to mechanistically simulate photosynthetic responses to VPD, but do not include information on soil moisture. Alternative indices of optical reflectance (the photochemical reflectance index, PRI[41,42] or the near-infrared reflectance of terrestrial vegetation, NIR_V[43]) and solar-induced fluorescence[44] add information about the effects of environmental stress on LUE, but their association with greenness changes poses a challenge to using them to estimate the independent effect of drought on photosynthesis[45,46]. Directly using soil moisture as an input to RS models has thus far been hampered by data availability with global coverage. New soil moisture data products that are based on microwave remote sensing[47] may resolve this constraint but are generally representative only for upper soil layers (which limits their applicability to deep-rooted vegetation) and are subject to data gaps in regions with dense vegetation cover[47]. Recent efforts to estimate root-zone

soil moisture[48] combined with estimates of the global distribution of plant rooting depth[49] may prove useful to address these limitations.

Using a global satellite data-driven GPP model, we have translated meteorological droughts (low precipitation) into soil moisture droughts and into more directly impact-relevant GPP drought events with extensive coverage in both space and time. Our results suggest that the influence of soil moisture substantially increases IAV in GPP and the size of GPP extreme events. However, our results suggest that even without accounting for the effect of increasing plant water-use efficiency[50] on soil moisture, drought impacts have not become more severe over the past three decades, and that there is no general global trend of increasing soil moisture limitation on GPP. This finding is in line with other studies[51,52,53].

We further found a compensatory role of water limitation in different regions that leads to a reduced apparent soil moisture effect on IAV in global GPP. This reflects earlier work[54,55] that found a declining importance of water availability on GPP and the land C balance when moving from local to global scales. However, we note that the model used for our analysis, as well as the one used by ref. [54], accounts for only relatively shallow soil water storage, without accounting for the possible role of other types of water storage that may be relevant for vegetation productivity (groundwater, for example), control its interannual variability and may preserve a strong soil moisture effect on C cycle variability at the global scale[56].

Our results highlight shortcomings in widely used[4,6,7,8] RS-based GPP estimates and contrast findings of increasing drought stress over past decades[6]. We have demonstrated that soil moisture is an important forcing of global vegetation primary production and interannual carbon cycle variability that cannot be replaced by information on atmospheric dryness and should therefore be accounted for in satellite data-driven estimates.

Methods

Observational data

GPP predictions by the RS models were compared to daily GPP estimates (aggregated to 8 d intervals) from the FLUXNET 2015 Tier 1 dataset (downloaded on 13 November, 2016). We use GPP based on the night-time partitioning method[59] (GPP_NT_VUT_REF). We filter negative daily GPP values, data for which more than 50% of the half-hourly data are gap-filled and for which the daytime and night-time partitioning methods (GPP_DT_VUT_REF and GPP_NT_VUT_REF, respectively) are inconsistent; that is, the upper and lower 2.5% quantiles of the difference between GPP values quantified by each method. The comparison is limited to data from 36 sites (see Supplementary Table 1 and Supplementary Fig. 1), where the effects of soil moisture is reliably identified[20], and to periods with clearly identified soil moisture effects based on ref. [20].

RS models

We use four RS global GPP models that also provide site-scale outputs for comparison to observations from FLUXNET sites.

MODIS MOD17A2H[3] (Version 6) is an empirical LUE model (see equation (1)), based on MODIS FPAR at 500 m resolution using 8 d periods. Biome-specific maximum LUE values are prescribed and multiplied by empirical stress functions to reduce GPP at high VPD and low temperature. Site-level data are extracted for the single pixel of the flux tower location at each site, using Google Earth Engine[60] and the gee_subset library[61].

BESS[25] is a process-based GPP model that uses remotely sensed data for the atmospheric state, land surface and air temperatures, leaf area index, spatially distributed CO_2 concentrations and canopy information (height, clumping). BESS explicitly simulates canopy radiative transfer, the surface energy balance and photosynthesis[62] using parameters for plant functional type-specific maximum carboxylation capacity (V_{cmax}). Original BESS outputs are given at a resolution of 1 km.

VPM[24] is an empirical LUE model (equation (1)) that is similar to MODIS, but driven by the remotely sensed MODIS Enhanced Vegetation Index (EVI from MOD09A1 C6, 500 m, 8 d) and reanalysis climate data. It distinguishes between C_3 and C_4 vegetation, modifies LUE by an extra water-stress scalar estimated by the Land Surface Water Index[63] and estimates absorption by chlorophyll specifically instead of absorption across a wider range of wavelengths (as implemented in MODIS and other RS models) by deriving fAPAR as a linear function of EVI. As in MODIS, VPM uses a temperature scalar to modify LUE, but does not use VPD data.

P-model[22] is a LUE model (equation (1)) in which LUE is internally predicted, varying over time and across space, on the basis of changing environmental conditions (monthly mean air temperature, VPD, elevation and CO_2 concentration) and on an optimality principle[64] that predicts stomatal conductance and foliar photosynthetic traits (including V_{cmax}) based on the standard model for C_3 plant photosynthesis[65]. The model thus does not rely on prescribed plant functional types or biome-specific parameters. For site-scale evaluations, the P-model is driven by MODIS FPAR (MCD15A3H Version 6, 500 m, 4 d) extracted using Google Earth Engine[60] and the gee_subset library[61] and meteorological data provided through the FLUXNET 2015 dataset. We have calibrated the apparent quantum yield efficiency parameter of the P-model, which acts as a linear scalar of LUE in equation (1), to observed GPP at high levels of soil moisture from the FLUXNET 2015 dataset. This yielded a value of 0.0579 (unitless, factor implicitly included in LUE).

Empirical soil moisture stress functions

We correct simulated GPP from different RS models (GPP_{mod}) using a set of empirical soil moisture stress functions ($\beta(\theta)$) as

$$\mathrm{GPP} = \beta(\theta)\,\mathrm{GPP}_{\mathrm{mod}}$$

We use data on the fLUE, estimated by ref. [20], to fit β functions ($\beta(\theta) \approx$ fLUE), based on two general patterns:

The functional form of $\beta(\theta)$ is general across all sites and can be approximated by a quadratic function that approaches 1 for soil moisture at a certain threshold θ^* and held constant at 1 for soil moisture values above that. Here θ is the plant-available soil water, expressed as a fraction of field capacity. The general form is:

$$\beta = \begin{cases} q(\theta - \theta^*)^2 + 1, & \theta \le \theta^* \\ 1, & \theta > \theta^* \end{cases} \qquad (2)$$

The sensitivity of $\beta(\theta)$ to extreme soil dryness ($\theta \to 0$) is correlated with the mean aridity at the site. The decrease in $\beta(\theta)$ associated with dryness is particularly strong at the driest sites (mostly deserts, grasslands and savannahs), whereas sites with intermediate aridity (mostly Mediterranean) have a smaller reduction in $\beta(\theta)$ when soil water becomes depleted. The sensitivity parameter q in equation (2) is defined by the maximum β reduction at low soil moisture $\beta_0 = \beta(\theta = \theta_0)$, leading to $q = (\beta_0 - 1)/(\theta^* - \theta_0)$ (see ref. 20). Note that q has a negative value. β_0 is modelled as a linear function of the mean aridity, quantified by the mean annual ratio of AET/PET, termed α':

$$\beta_0 = p_0 + p_1 \alpha' \qquad (3)$$

Note that θ_0 and θ^* differ slightly between approaches, and that α' relates to α in the Priestley–Taylor equation[65] as $\alpha' = \alpha / 1.26$.

We have tested several approaches to fit parameters p_0 and p_1 for empirical soil moisture stress functions $\beta(\theta)$. Final fitted functions based on different approaches bracket the fLUE values derived at our selected sites (group 1 in Supplementary Table 1, Supplementary Fig. 6). More information on the fitting procedure and parameter values are given in Supplementary Section 5. Three parameterizations of β functions were used to estimate uncertainty in the sensitivity of $\beta(\theta)$: β_a for low sensitivity, β_b for intermediate sensitivity and distinguishing parameters between woody and herbaceous vegetation, and β_c for high sensitivity.

Global P-model simulations

We developed a new P-model implementation to estimate GPP for global and site-level simulations within the same modelling framework (model code SOFUN v1.1.0)[66]. Global simulations are performed here for years 1982–2016

and are driven by FPAR3g data[27] for fAPAR; WATCH-WFDEI elevation and climate data[67] for temperature, shortwave radiation, and specific humidity, converted to VPD (see the Supplementary Information); and measured globally uniform atmospheric CO_2 concentrations. The β functions were applied to daily GPP, calculated on the basis of soil moisture simulated by the SPLASH model[23], which is implemented within the global SOFUN modelling framework[13]. The soil moisture model is forced by WATCH-WFDEI precipitation as input and estimates PET based on the Priestley–Taylor equation. The soil water balance is determined on the basis of a spatially varying plant-available soil water holding capacity (Supplementary Fig. 12), derived from SoilGrids[26] data for texture and soil depth (see also Supplementary Section 5.4). Four simulations were carried out: s0, without soil moisture effects; s1a, using β_a; s1b, using β_b; and s1c, using β_c.

Mapping contributing regions

We adopted and modified the method proposed by ref. [56] and calculated an index f based on equation (1) of their paper to quantify the fractional contribution of each grid cell to the amplification of GPP IAV through soil moisture effects:

$$f_j = \frac{\sum_t \frac{x_{jt}|X_t|}{X_t}}{\sum_t |X_t|} \qquad (4)$$

Here, x_{jt} is the difference in the detrended annual GPP of grid cell j and year t that is caused by the effects of soil moisture, calculated as the difference in detrended annual GPP in simulations s1b and s0. X_t is the global detrended annual GPP in simulation s1b.

Identification of GPP extreme events

GPP extreme events were identified following the method proposed by ref. [57] as contiguous domains in longitude–latitude–time space, where the monthly detrended GPP anomaly from its mean seasonal cycle is below the 2% quantile of all anomaly values within the respective continent. The domains are determined based on simulation s1b using the R package neuroim[68]. The impacts of events were calculated for each simulation (s0 and s1b) as the monthly detrended GPP anomaly relative to the mean seasonal cycle in the respective simulation, cumulated over the domain (grid cells and months) of the respective event.

Code availability

Reproducible code is available via github (https://github.com/stineb/soilm_global) and published on Zenodo at https://doi.org/10.5281/zenodo.2543324.

Data availability

P-model outputs from site-scale and global simulations are available on Zenodo at: https://doi.org/10.5281/zenodo.1423484.

References

1. Ciais, P. et al. Europe-wide reduction in primary productivity caused by the heat and drought in 2003. Nature 437, 529–533 (2005). 2. Zhang, Y. et al. Development of a coupled carbon and water model for estimating global gross primary productivity and evapotranspiration based on eddy fux and remote sensing data. Agric. For. Meteorol. 223, 116–131 (2016). 3. Running, S. W. et al. A continuous satellite-derived measure of global terrestrial primary production. BioScience 54, 547–560 (2004). 4. Zhao, M. & Running, S. W. Drought-induced reduction in global terrestrial net primary production from 2000 through 2009. Science 329, 940–943 (2010). 5. Zhang, Y. et al. Canopy and physiological controls of GPP during drought and heat wave. Geophys. Res. Lett. 43, 3325–3333 (2016). 6. Schwalm, C. R. et al. Global patterns of drought recovery. Nature 548, 202–205 (2017). 7. Ballantyne, A. et al. Accelerating net terrestrial carbon uptake during the warming hiatus due to reduced respiration. Nat. Clim. Change 7, 148–152 (2017). 8. Liu, Z. et al. Precipitation thresholds regulate net carbon exchange at the continental scale. Nat. Commun. 9, 3596 (2018). 9. Monteith, J. L. Solar radiation and productivity in tropical ecosystems. J. Appl. Ecol. 9, 747–766 (1972). 10. Cowan, I. R. & Farquhar, G. D. Stomatal function in relation to leaf metabolism and environment. Symp. Soc. Exp. Biol. 31, 471–505 (1977). 11. Martínez-Vilalta, J., Poyatos, R., Aguadé, D., Retana, J. & Mencuccini, M. A new look at water transport regulation in plants. New Phytol. 204, 105–115 (2014). 12. Sperry, J. S. et al. Predicting stomatal responses to the environment from the optimization of photosynthetic gain and hydraulic cost. Plant Cell Environ. 40, 816–830 (2017). 13. Stocker, B. sofun v1.1.0 (2018); https://doi.org/10.5281/zenodo.1213758. 14. Ruddell, B. L. & Kumar, P. Ecohydrologic process networks: 1. Identifcation. Water Resour. Res. https://doi.org/10.1029/2008WR007279 (2009). 15. Seneviratne, S. I. et al. Investigating soil moisture–climate interactions in a changing climate: A review. Earth Sci. Rev. 99, 125–161 (2010). 16. Goerner, A., Reichstein, M. & Rambal, S. Tracking seasonal drought efects on ecosystem light use efciency with satellite-based PRI in a Mediterranean forest. Remote. Sens. Environ. 113, 1101–1111 (2009). 17. Novick, K. A. et al. Te increasing importance of atmospheric demand for ecosystem water and carbon fuxes. Nat. Clim. Change 6, 1023–1027 (2016). 18. Sulman, B. N. et al. High atmospheric demand for water can limit forest carbon uptake and transpiration as severely as dry soil. Geophys. Res. Lett. 43, 2016GL069416 (2016). 19. Rogers, A. et al. A roadmap for improving the representation of photosynthesis in Earth system models. New Phytol. 213, 22–42 (2017). 20. Stocker, B. D. et al. Quantifying soil moisture impacts on light use efciency across biomes. New Phytol. 218, 1430–1449 (2018). 21. Egea, G., Verhoef, A. & Vidale, P. L. Towards an improved and more fexible representation of

water stress in coupled photosynthesis–stomatal conductance models. Agric. For. Meteorol. 151, 1370–1384 (2011). 22. Wang, H. et al. Towards a universal model for carbon dioxide uptake by plants. Nat. Plants 3, 734–741 (2017). 23. Davis, T. W. et al. Simple process-led algorithms for simulating habitats (SPLASH v.1.0): robust indices of radiation, evapotranspiration and plant-available moisture. Geosci. Model Dev. 10, 689–708 (2017). 24. Zhang, Y. et al. A global moderate resolution dataset of gross primary production of vegetation for 2000–2016. Sci. Data 4, 170165 (2017). 25. Jiang, C. & Ryu, Y. Multi-scale evaluation of global gross primary productivity and evapotranspiration products derived from breathing earth system simulator (BESS). Remote. Sens. Environ. 186, 528–547 (2016). 26. Hengl, T. et al. SoilGrids1km–global soil information based on automated mapping. PLoS ONE 9, e105992 (2014). 27. Zhu, Z. et al. Global data sets of vegetation leaf area index (LAI)3g and fraction of photosynthetically active radiation (FPAR)3g derived from global inventory modeling and mapping Studies (GIMMS) Normalized Diference Vegetation Index (NDVI3g) for the Period 1981 to 2011. Remote Sensing 5, 927–948 (2013). 28. Reichstein, M. et al. Climate extremes and the carbon cycle. Nature 500, 287–295 (2013). 29. Zscheischler, J. et al. A few extreme events dominate global interannual variability in gross primary production. Environ. Res. Lett. 9, 035001 (2014). 30. Turner, D. P. et al. Site-level evaluation of satellite-based global terrestrial gross primary production and net primary production monitoring. Glob. Change Biol. 11, 666–684 (2005). 31. Leuning, R., Cleugh, H. A., Zegelin, S. J. & Hughes, D. Carbon and water fuxes over a temperate Eucalyptus forest and a tropical wet/dry savanna in Australia: measurements and comparison with MODIS remote sensing estimates. Agric. For. Meteorol. 129, 151–173 (2005). 32. Mu, Q. et al. Evaluating water stress controls on primary production in biogeochemical and remote sensing based models. J. Geophys. Res. Biogeosci. 112, G01002 (2007). 33. Sims, D. A., Brzostek, E. R., Rahman, A. F., Dragoni, D. & Phillips, R. P. An improved approach for remotely sensing water stress impacts on forest C uptake. Glob. Change Biol. 20, 2856–2866 (2014). 34. Migliavacca, M. et al. Seasonal and interannual patterns of carbon and water fuxes of a poplar plantation under peculiar eco-climatic conditions. Agric. For. Meteorol. 149, 1460–1476 (2009). 35. Koirala, S. et al. Global distribution of groundwater-vegetation spatial covariation. Geophys. Res. Lett. 44, 4134–4142 (2017). 36. Sperry, J. S. & Love, D. M. What plant hydraulics can tell us about responses to climate-change droughts. New Phytol. 207, 14–27 (2015). 37. Biederman, J. A. et al. CO2 exchange and evapotranspiration across dryland ecosystems of southwestern North America. Glob. Chang. Biol. 23, 4204–4221 (2017). 38. Quéré, C. L. et al. Global carbon budget 2017. earth system science. Data 10, 405–448 (2018). 39. Xiao, X. et al. Satellite-based modeling of gross primary production in an evergreen needleleaf forest. Remote Sens. Environ. 89, 519–534 (2004). 40. Mahadevan, P. et al. A satellite-based biosphere parameterization for net ecosystem CO2 exchange: Vegetation Photosynthesis and Respiration Model (VPRM). Glob. Biogeochem. Cycles

https://doi.org/10.1029/2006GB002735 (2008). 41. Gamon, J. A., Peñuelas, J. & Field, C. B. A narrow-waveband spectral index that tracks diurnal changes in photosynthetic efciency. Remote Sens. Environ. 41, 35–44 (1992). 42. Penuelas, J., Filella, I. & Gamon, J. A. Assessment of photosynthetic radiation-use efciency with spectral refectance. New Phytol. 131, 291–296 (1995). 43. Badgley, G., Field, C. B. & Berry, J. A. Canopy near-infrared refectance and terrestrial photosynthesis. Sci. Adv. 3, e1602244 (2017). 44. Porcar-Castell, A. et al. Linking chlorophyll a fuorescence to photosynthesis for remote sensing applications: mechanisms and challenges. J. Exp. Bot. 65, 4065 (2014). 45. Vicca, S. et al. Remotely-sensed detection of efects of extreme droughts on gross primary production. Sci. Rep. 6, 28269 (2016). 46. He, M. et al. Satellite detection of soil moisture related water stress impacts on ecosystem productivity using the MODIS-based photochemical refectance index. Remote Sens. Environ. 186, 173–183 (2016). 47. Dorigo, W. et al. ESA CCI soil moisture for improved earth system understanding: state-of-the art and future directions. Remote Sens. Environ. 203, 185–215 (2017). 48. Mohanty, B. P., Cosh, M. H., Lakshmi, V. & Montzka, C. Soil moisture remote sensing: state-of-the-science. Vadose Zone J. 16, 0 (2017). 49. Fan, Y., Miguez-Macho, G., Jobbágy, E. G., Jackson, R. B. & Otero-Casal, C. Hydrologic regulation of plant rooting depth. Proc. Natl Acad. Sci. USA 114, 10572–10577 (2017). 50. Keeling, R. F. et al. Atmospheric evidence for a global secular increase in carbon isotopic discrimination of land photosynthesis. Proc. Natl Acad. Sci. USA 114, 10361–10366 (2017). 51. Shefeld, J., Wood, E. F. & Roderick, M. L. Little change in global drought over the past 60 years. Nature 491, 435–438 (2012). 52. Berg, A. & Shefeld, J. Climate change and drought: the soil moisture perspective. Curr. Clim. Change Rep. https://doi.org/10.1007/s40641-018- 0095-0 (2018). 53. Hao, Z., AghaKouchak, A., Nakhjiri, N. & Farahmand, A. Global integrated drought monitoring and prediction system. Sci. Data 1, 140001 (2014). 54. Jung, M. et al. Compensatory water efects link yearly global land CO2 sink changes to temperature. Nature 541, 516–520 (2017). 55. Ahlström, A. et al. Te dominant role of semi-arid ecosystems in the trend and variability of the land CO2 sink. Science 348, 895–899 (2015). 56. Humphrey, V. et al. Sensitivity of atmospheric CO2 growth rate to observed changes in terrestrial water storage. Nature 560, 628–631 (2018). 57. Zscheischler, J., Mahecha, M. D., Harmeling, S. & Reichstein, M. Detection and attribution of large spatiotemporal extreme events in earth observation data. Ecol. Inform. 15, 66–73 (2013). 58. Gillespie, C. S. Fitting heavy tailed distributions: the powerlaw package. J. Stat. Sofw. https://doi.org/10.18637/jss.v064.i02 (2015).

Acknowledgments

We thank C. Jian and Y. Ryu for sharing BESS model outputs, and Y. Zhang for sharing VPM model outputs and all for supporting the use and interpretation of their data. We thank Z. Zhu for sharing updated FPAR3g data, D. Sandoval Calle for preparing soil data, and W. Han, R. Thomas and T.

Davis for their contributions to the development of the P-model. B.D.S. was funded by ERC Marie Sklodowska-Curie fellowship H2020- MSCA-IF-2015, project FIBER, grant no. 701329. J.P. was funded by ERC Synergy grant no. ERC-SyG-2013-610028 IMBALANCE-P, the Spanish Government grant no. CGL2016-79835-P and the Catalan Government grant SGR-2017-1005. T.F.K was supported by the NASA Terrestrial Ecology Program IDS Award No. NNH17AE86I. This work is a contribution to the AXA Chair Programme in Biosphere and Climate Impacts and the Imperial College initiative on Grand Challenges in Ecosystems and the Environment (I.C.P.). S.I.S acknowledges support from the EU FP7 programme, through the ERC DROUGHT-HEAT project (contract no. 617518). This work used eddy covariance data acquired and shared by the FLUXNET community, including these networks: AmeriFlux, AfriFlux, AsiaFlux, CarboAfrica, CarboEuropeIP, CarboItaly, CarboMont, ChinaFlux, Fluxnet-Canada, GreenGrass, ICOS, KoFlux, LBA, NECC, OzFlux-TERN, TCOS-Siberia and USCCC. The processing and harmonization of the FLUXNET eddy covariance data was carried out by the European Fluxes Database Cluster, AmeriFlux Management Project and the Fluxdata project of FLUXNET, with the support of the CDIAC and ICOS Ecosystem Thematic Center, and the OzFlux, ChinaFlux and AsiaFlux offices.